UNIVERSITY OF BIRMINGHAM

University of Birmingham
Research at Birmingham

Microstructural and texture development in direct laser fabricated IN718

Parimi, Lakshmi L.; A., Ravi G.; Clark, Daniel; Attallah, Moataz M.

[Link to publication on Research at Birmingham portal](#)

Microstructural and texture development in direct laser fabricated IN718☆

CrossMark

Lakshmi L. Parimi[a], Ravi G. A.[a], Daniel Clark[b], Moataz M. Attallah[a],*

[a]School of Metallurgy and Materials, University of Birmingham, Edgbaston, Birmingham, B15 2TT, UK
[b]Rolls-Royce plc, P.O. Box 31, Derby DE24 8BJ, UK

ARTICLE DATA

ABSTRACT

Microstructural characterisation was performed for IN718 thin-walled builds, produced using direct laser fabrication (DLF), to understand the influence of the variations in the deposition path and the laser power on the microtexture, grain structures and intermetallic particle morphology development. Considerable differences were observed, with the high laser power input generating a columnar grain structure, with a strong <001> fibre texture along the build height, compared to a mixture of fine uniform and large columnar grains in the low power builds, with a near random texture. The influence of different DLF conditions on the formation of Laves and of δ phase was also found to be significant, with the Laves phase precipitates being larger in the high laser power sample. Carbides and δ were also present in the high power build, but were not observed in the low power samples regardless of the deposition path.

1. Introduction

Direct laser fabrication (DLF) is a near net shaping technique where three-dimensional components are produced layer-by-layer by consolidating powder using a focused laser heat source. Over the past decade, DLF has shown to be capable of producing components with complex geometries to near net-shape, with considerable cost and material savings for low batch runs in Ni-base superalloys [1–3]. One of the major drawbacks in the process is the bonding defects and porosity in the builds, as well as the creation of heterogeneous microstructure, which resulted in extensive work being undertaken in the past decades to produce structurally-sound builds with acceptable mechanical properties [4,5]. Although sound builds could be produced using DLF, their mechanical properties were poor compared to wrought products [4–6], which highlights the influence of the microstructure. Generally, the builds were reported to have a columnar grain structure, growing epitaxially from the substrate, with the orientation of the grains being strongly influenced by the deposition strategy [7]. Some builds were found to have a banded grain structure with alternate coarse and fine grain bands due to different cooling rates, where the fine grains are typically found in the locations associated with rapid cooling rates [4,8]. Furthermore, the build direction appears to influence the mechanical properties, whereby the tensile strength along the deposition direction was found to be ~55–60% higher than across the build direction in IN718 builds [5]. Although limited work is available in the literature on the effect of this deposition strategy on the build microstructure, it is important to understand the grain size distribution and texture between the layers in detail [7]. With respect to the texture development, it was previously reported that IN718

  * Corresponding author. Tel.: +44 121 4147842; fax: +44 121 4147890.
    E-mail address: M.M.Attallah@Bham.ac.uk (M.M. Attallah).

builds have a banded microstructure with random texture in IN718 builds [4]. Nonetheless, limited work is done previously on the influence of the laser power (a key process parameter) on the build microstructure and texture development [9].

IN718 is a $\gamma' + \gamma''$-strengthened Ni-superalloy [10]. It is generally less prone to solid-state cracking (e.g. strain age/reheat cracking) than γ'-strengthened alloys due to the relatively sluggish γ'' precipitation kinetics, which makes it suitable for DLF [6,11]. Nonetheless, IN718 is prone to the formation of Laves phases at elevated temperatures, whereas long thermal exposures lead to the formation of precipitates of the brittle δ phase which can act as stress raisers [12]. Segregation of Nb leading to the formation of Laves phase was previously observed in IN718 DLF builds [6,13], but the influence of the process parameters on the morphology and the density/volume fraction of these phases was not studied. It is believed that the as-fabricated builds typically have poor mechanical properties compared to the wrought products due in part to these detrimental phases. Qi et al. showed that the mechanical properties can be improved by performing a homogenisation heat treatment at ~1100 °C for 1–2 h, followed by a solution and aging treatment for precipitation of strengthening γ' and γ'' phases [13]. It is conceivable that the parameters that influence the thermal cycle during DLF (e.g. the deposition path and laser power) might also influence the formation and morphology of these detrimental phases, making it possible to tailor a microstructure with good properties by controlling the parameters.

In the present investigation, the development of texture, the grain structure and particle morphology will be investigated in IN718 builds, focusing on the influence of the deposition path (unidirectional or bidirectional), as well as the use of high laser power on the dendrite orientation and texture. The aim of the study is to assess the different microstructures that can be formed due to DLF of IN718, in order to identify the sensitivity of the grain and precipitate morphology to the variations in the process parameters (mainly the scanning strategy and the laser power).

2. Materials and Methods

Commercially available gas-atomised IN718 powder was used in this investigation, with the chemical composition given in Table 1. The average particle size of the powder is ~60 μm, with 90% of the particles falling within the size range of 40–100 μm, which is the typical range used for DLF [13]. The powder particles are mostly spherical in shape, with internal porosity infrequently observed in the particles and very fine satellite particles attached to the particles (Fig. 1a). The microstructure of the particles shows a fine dendritic network, which is caused by the rapid solidification during gas atomisation (Fig. 1b). The powder was used to build straight, single bead-width, thin-walled samples of dimensions 20 mm × 0.7 mm × 10 mm (x, y, z) to simulate the repair application of DLF. A Quantum DLF

machine, fitted with a Wegmann–Baasel CO_2 laser (maximum power of 1750 W), was used to deposit the builds in an argon atmosphere within a glove box, with the O_2 level being kept under 50 ppm. The Z-increment (the vertical spacing between the successive build layers) was kept at 0.3 mm throughout the build. The laser beam was focused to a spot size of 0.7 mm using a ZnSe lens, with a focal length of 127 mm. A four-beam nozzle assembly was used for powder feeding, where the powder focus was set to coincide with the laser beam focus which is ~3–4 mm from the substrate, using argon both as a carrier gas with a flow rate of 5.5 l/min and a nozzle gas to protect the lens from the rebounding particles from the build.

Identification of the process parameter window was performed by depositing a series of specimens, varying the laser power between 300 and 500 W, scan speed between 200 and 400 mm/min and powder flow rate between 18 and 55 g/min. Following the identification of the process window, four thin-walled builds were deposited for each condition. The dimensions of the builds were found to be within ±200 μm from the target dimensions for all the conditions. Although this is beyond the scope of this paper, the authors have investigated deposition scaling up to 2 mm thick walls and 10 mm wide solid blocks (deposited with several beads). Generally speaking, the structural and geometrical integrity becomes more difficult to control with the increase in the wall width.

Builds which did not show any cracking or bonding defects, either between the individual layers or between the build and the substrate, were chosen for further microstructural studies. In this particular study, three conditions from the above, which produced sound builds were investigated in order to understand the influence of the deposition path and the laser power on the microstructural development. With the first two conditions the effect of deposition path on the microstructure was studied keeping the other process parameters constant (laser power of 390 W, laser scan speed 200 mm/min, and powder flow rate 18 g/min). The two builds were performed using a unidirectional (B1) and a bidirectional (B2) deposition path (Fig. 2). In B1 the laser was switched off between the layers for a time equal to deposition of one layer (~6 s). Also, during this laser off time, the laser head moved back to the initial position with powder flow continuing stably and the carrier gas continuing to flow cool gas across the deposit. In B2 the laser beam continuously moved back and forth for deposition, which reduces the time available for cooling (in the wake of the laser beam), with no forced cooling between the layers as in B1. A third build (B3) was deposited using a bidirectional deposition path to understand the influence of laser power on the build microstructure. In order to see a significant effect a considerably higher laser power (910 W) was used. To ensure that the build did not contact the nozzle in B3 condition, the powder feed rate was reduced to 7 g/min. The aim of this reduction in feed rate is to prevent the uppermost built layers (melt pool) from approaching the nozzle due to the enhanced powder catchment efficiency caused by the increase in melt pool dimensions with the increase in laser power.

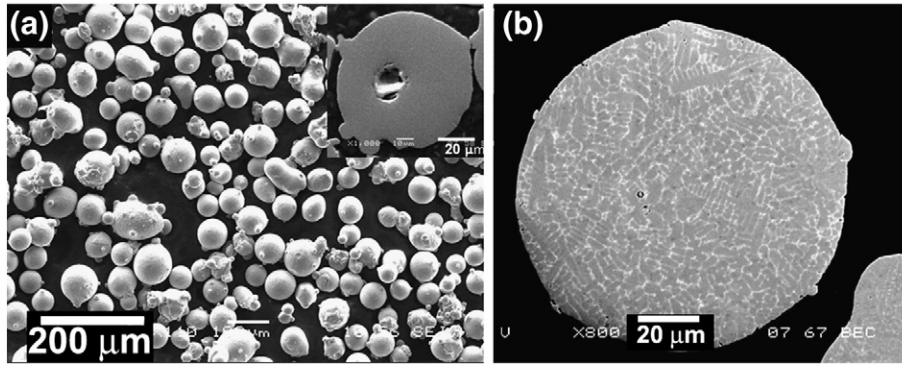| Table 1 – Chemical composition of the base IN718 powder.											
Element	Ni	Cr	Fe	Nb	Mo	Ti	Al	C	B	O	Si
wt.%	53.34	18.2	18.9	5.1	3.1	0.9	0.29	0.021	0.005	0.004	0.14

Fig. 1 – Micrographs for the (a) morphology of the gas atomised IN718 powder, with the insert showing a cross section of a powder particle with internal porosity, and (b) backscattered electron (BSe) micrograph for the powder microstructure showing a fine dendritic network.

Following the DLF, the builds were mounted in bakelite, ground and polished to 0.05 μm oxide alumina finish. Porosity measurements were conducted on polished specimens, by performing image analysis of optical micrographs. The specimens were later etched using Kallings reagent (5 g $CuCl_2$ in 100 ml HCl and 100 ml distilled H_2O) to investigate the microstructure using optical and scanning electron microscopy (SEM). Electrolytic etching was also used to reveal the precipitates, using a 10% vol. H_3PO_4 in H_2O for 5 s at 5 V.

Microstructural investigations were performed using an FEI-Sirion field emission gun scanning electron microscope (FEG-SEM), equipped with a backscattered electron (BSE) detector, and an HKL electron backscattered diffraction (EBSD) detector, with Channel 5 software for EBSD acquisition and analysis. Additional investigations were performed in a JEOL 7000 FEG-SEM, equipped with an energy-dispersive X-ray spectroscopy (EDS) detector.

3. Results and Discussion

3.1. Porosity

Porosity measurements were performed for the three conditions by taking series of images across the build in a 5 mm × 5 mm area. Spherical pores were observed in all three builds, which were scattered throughout the build. Both low-power

builds B1 and B2 displayed a porosity of 0.2 ± 0.1% as shown in Fig. 3a, b, compared to ~0.8 ± 0.2% (Fig. 3c) in the high power build. This shows that the tool path does not appear to have a strong influence on porosity, but the laser power does. It is known that the porosities in DLF builds can be attributed either to the porosity originally present in GA powder [13], or created during the process within the melt pool as a result of molten metal fluidity or turbulence (due to excessive superheat [14]). The pore size varied from 40 to 100 μm, which is bigger than the porosity observed in the powder, which suggests that the pores formed due to the turbulences in the melt pool caused by the interaction between the powder particles and the laser. From pore images, which are spherical, such as that shown in (Fig. 3d) it can be inferred that the porosity is due to gas entrapment. The use of high laser power would increase the melt pool temperature, decrease the molten metal viscosity, and increase turbulence in the melt pool and thus increase the extent of gas-entrapment in the build [9]. The fluidity would also relate to the inter-pass temperature and time for heat dissipation between passes.

3.2. Grain morphology

Optical micrographs of B1, B2, and B3 of the X–Z plane (per the notation in Fig. 2) are shown in Fig. 4. The microstructure of the as-deposited samples showed a layered structure with a thin demarcation at the interface between the layers (shown with
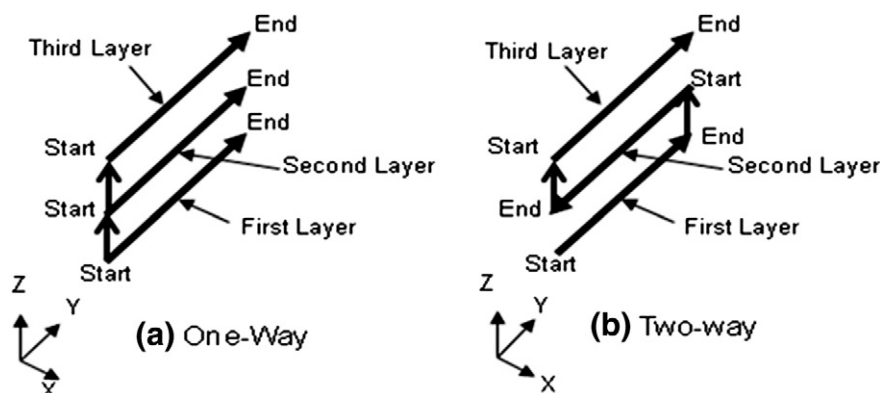

Fig. 2 – Schematic diagrams showing the investigated deposition strategies: (a) unidirectional (B1) and (b) bidirectional (B2).
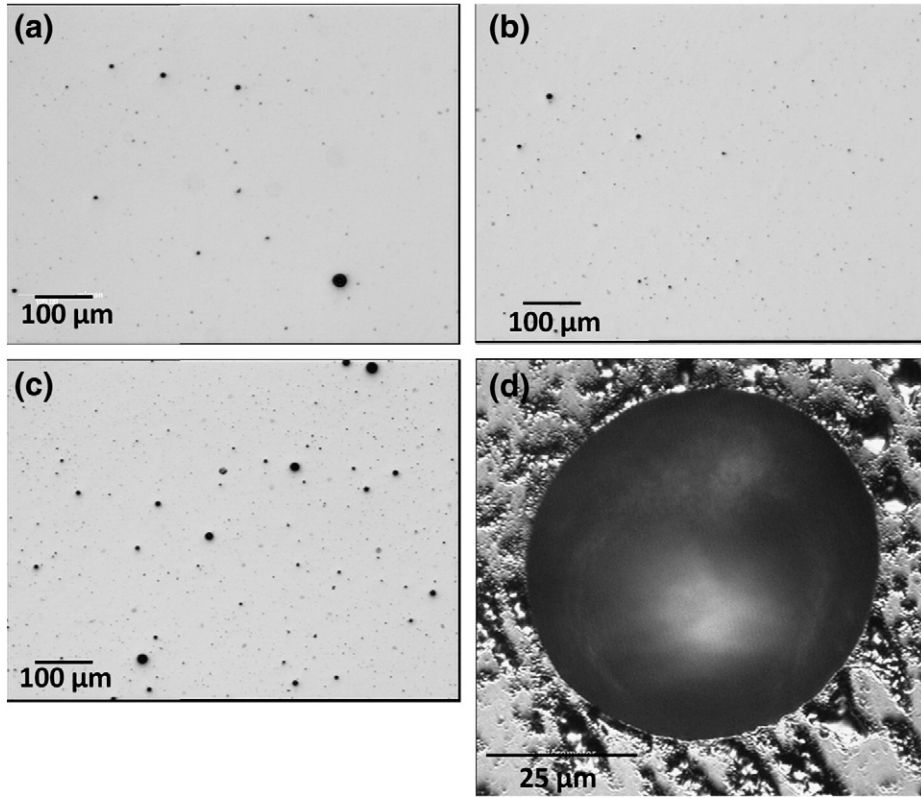
Fig. 3 – Porosity distribution in the samples in (a) the unidirectional/B1 build, (b) the bidirectional B2 build, (c) the high power B3 build, and (d) a micrograph for a typical pore in the build.

arrows in Fig. 4a, b). This demarcation was more prominent in unidirectional deposition than in bidirectional deposition. The size of the layers (i.e., the mean track height) was around

350 μm for both B1 and B2 deposits. Each layer contained aligned dendrites, which were contained within the layers and did not grow across the layers for lower power deposits B1 and

Fig. 4 – Optical micrographs showing the dendrites orientation and layer demarcation in (a) unidirectional deposition (B1), and (b) bidirectional deposition (B2), both built using similar process parameters, (c) high power condition (B3), and (d) schematic illustrations of the heat flux directions (not to scale).

B2. The dendrite arm spacing (DAS) [15] was relatively fine (~5 μm) compared to the typical DAS in cast microstructures (10 μm–40 μm), which can be attributed to the rapid cooling rate during DLF (10^2–10^3 K s^{-1}) [9].
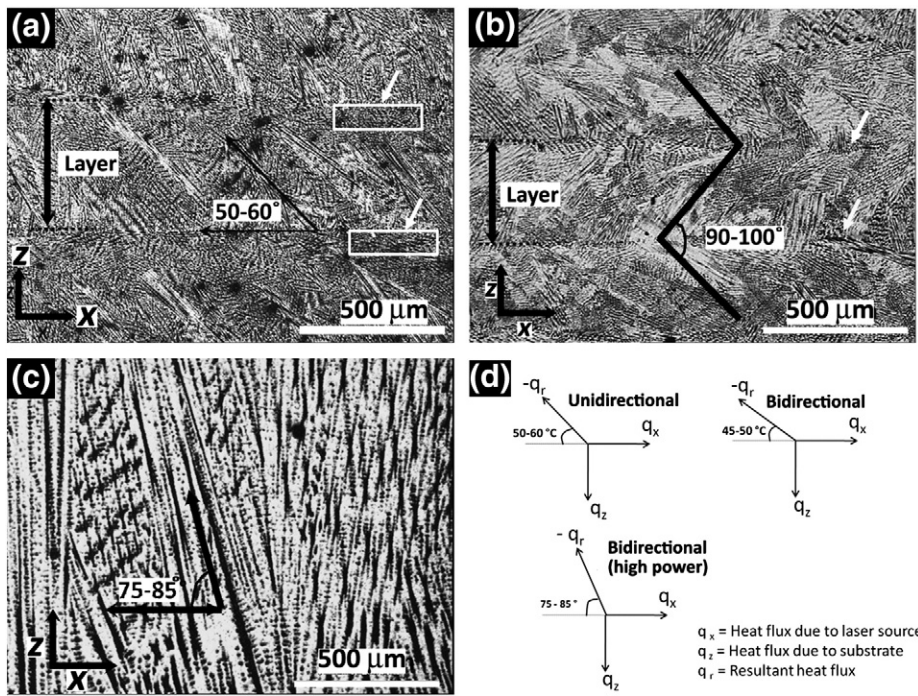
Comparing the builds, significant microstructural differences, especially with respect to the dendrite growth morphology, were observed. In B1, the dendrites were unidirectionally oriented at an angle of ~50°–60° to the substrate in all the layers (Fig. 4a), with the inclination tracking the rear of the melt pool, whereas the dendrites were oriented in a zigzag fashion in B2, and intersecting at the interface between the layers at an angle of ~90°–100° (Fig. 4b). In both cases, the dendrites were oriented along the moving heat source. In the case of B3 (Fig. 4-c), the dendrites were oriented at angle of ~75°–85° to the substrate. This dendrite orientation can be related to the influence of the vertical and horizontal heat fluxes (q_x and q_z, respectively), as well as the dendrite orientation of the previously deposited layers (Fig. 4d). If q_x is the horizontal heat flux due to the moving heat source, and q_z is the vertical heat flux due to the heat sink effect by the substrate, then q_r is the resultant heat flux, which is along the dendrite growth direction.

The difference in grain orientation between B1, B2, and B3 can be attributed to the variation in the contribution of q_x and q_z

with the change in the deposition path. Since the laser is continuously switched on throughout the deposition process in B2, this results in more heat accumulation (i.e., thermal energy) in B2 than in B1 where the laser is switched off between the layers, as previously explained. As a result, the temperature at the starting point of layer ($n + 1$) (following the completion of layer n deposition, and just before starting layer $n + 1$) would be lower in B1 compared to B2 due to the aforementioned differences in the thermal boundary conditions. Although the temperature difference was not measured in this study, this difference is believed to be ~400 °C, based on the predictions of a finite element model validated for the used DLF system (which will be discussed in a separate paper). Moreover, the change in the dendrite orientation across the layers depends on the dendrite orientation in the previous layer. As the dendrites tend to grow perpendicular to the previous layers of dendrites, this makes them oriented more towards the q_r direction [7].

Further examination in the grain structures revealed that a banded structure existed, with very fine grains forming at the inter-layer interface. In B1, the size of the fine grain band was observed to be around 40 μm thick (Fig. 5-a) and the size of the columnar grains contained within the layer was ~150 × 50 μm, with an aspect ratio of ~3. The fine grains between layers
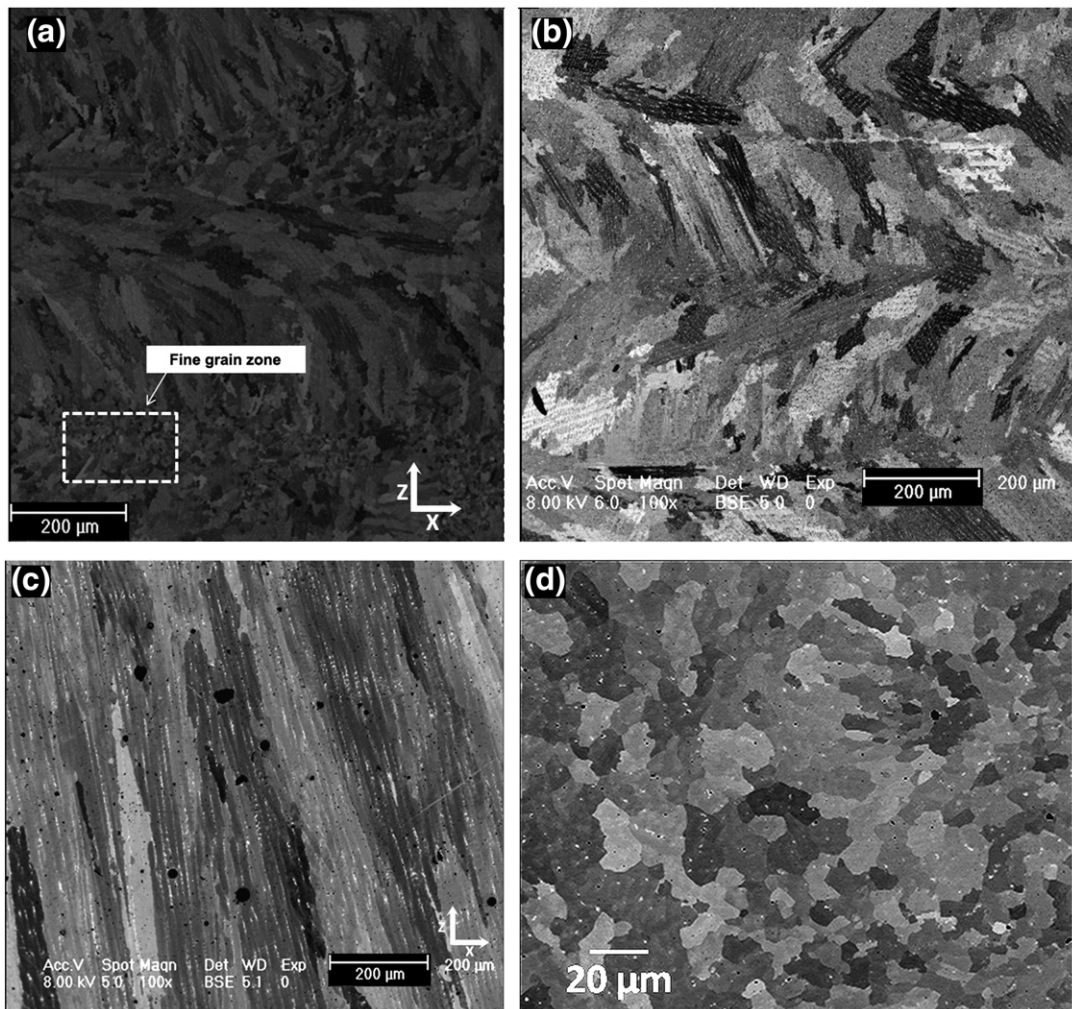

Fig. 5 – BSE SEM micrographs showing the grain structure in (a) B1 (clearly showing the equiaxed grain region between the layers), (b) B2, (c) B3, and (d) showing the fine grain zone in B1.

were 10–20 μm (equivalent circle diameter), with an aspect ratio of ~1.5 (Fig. 5-d showing magnified fine grain zone of Fig. 5-a). Although B2 (Fig. 5-b) also showed a banded structure, the fine grain zone was not as prominent as in B1. The average maximum ferret of the grains inside the layer for B2 was ~100–200 μm with an aspect ratio of ~2. Because the laser is switched off between the layers in B1, each layer had a reasonable time to cool before another layer is deposited, which led to the formation of the fine grain zone between layers. Conversely, this fine grain zone is not as prominent in B2 since the laser beam was switched on throughout the process, with the total time taken to deposit two layers being less than that in B1, so that the extent of cooling between layers is less. This fine grain zone was very obvious in the first few layers for both B1 and B2 builds, but was not obvious near the top of the builds, which is presumably because the substrate initially acts as an efficient heat sink, similar to the chill zone effect in the castings.

By increasing the laser power (B3), the grains were found to increase in length (Fig. 5c), with the dendrites being aligned at an angle of ~80° to the substrate, suggesting that the resultant heat flux is almost vertical. Furthermore, the demarcation between the layers was not observed as in the case of B1 and B2 (Fig. 5a, b). It is clear that the heat input was high enough in B3 for the grains to grow epitaxially from the previous layer, rather than by re-nucleating across the layers. It is evident that the continuous high power heating in B3 increased the melt pool temperature, which influenced the thermal gradient and hence the primary axis of the grain growth. This resulted in the creation of long columnar grains (2–3 mm long, with an aspect ratio of ~30) in the plane of sectioning. It is clear that the different deposition strategies and the high laser power resulted in considerable microstructural changes in the grain size and morphology in the plane of sectioning.

The deposits would have different thermal histories at different locations of the build which would influence the microstructure. Fig. 6 shows the schematic representation of the grain orientation in the entire deposit along the central axis examined for the three deposits. The variation in the dendrite structure was schematically plotted based on the optical and scanning electron (SE) microscopes for the entire build. For the low power builds i.e., in B1 and B2 there was a little variation in the dendrite orientation (except for the edge of the build, which showed slightly more vertically oriented grains). For the higher laser power setting, the grains tended

to grow from end faces to the centre while at the ends of the deposit the grains were almost vertical. The dotted boxes in Fig. 6 show the locations from which the EBSD maps were taken.

3.3. Texture

EBSD mapping was performed across the length of the build, covering a relatively large area (1 mm × 5 mm) at the centre of the build (Fig. 7). The B1 sample was found to have a banded grain structure, with fine grain zones at the interface between the layers that contained inclined columnar grains (Fig. 7a). The width of the fine grains zone was found to decrease from the bottom upwards. The fine grain band size was around 150–200 μm at the base and decreased to 20 μm at the top (5 mm from base) of the build (marked by boxes in Fig. 7a) because the melt pool temperature will increase as the conduction from the build to the substrate becomes less significant. Furthermore, the fine grain regions were generally found to have a more random texture than the columnar grains (mainly <001> and less frequently <101> oriented grains along the y-direction), although the overall texture of the entire build appeared to be a complex composite cluster of textures with an overall random texture. The Inverse Pole Figure (IPF) map of B2 also showed a banded structure with randomly oriented grains (Fig. 7b). This banded structure was previously observed by Blackwell [4], where it was attributed to the high thermal conductivity of Ni-superalloys that leads to rapid cooling during DLF, suppressing the epitaxial growth. In B3 (Fig. 7c), the build initially started with the small columnar grains, progressing to very large columnar grains along the build. The demarcation in the final layer was very clear with the small columnar grains.

It is known that solidification under varying conditions leads to three different grain morphologies, 1) fully columnar, 2) columnar plus equiaxed, and 3) fully equiaxed. Different morphologies can be obtained by controlling the thermal gradient (G) and the solidification rate (R), using the process parameters like laser power, travel speed, substrate temperature and beam diameter. These affect the G and R values, resulting in a variation in the grain morphology of the laser deposited sample. Process maps were developed by Gäumann et al. to predict the transition from equiaxed to columnar microstructure based on Hunt's model for columnar and equiaxed
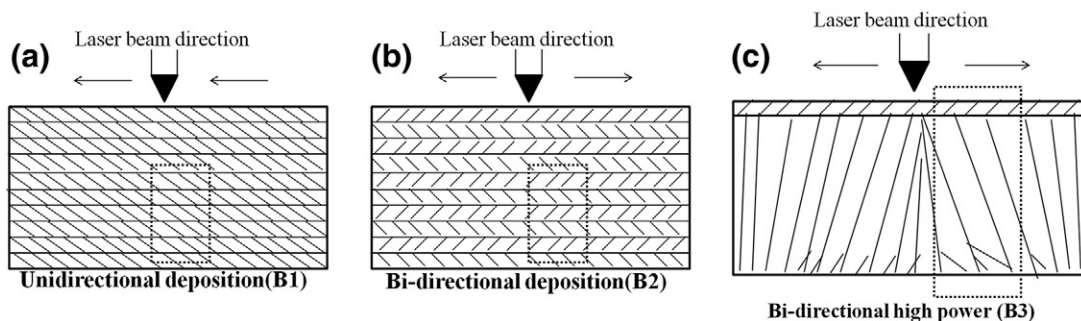

Fig. 6 – Schematic showing the dendrite/grain orientation of the entire build in unidirectional deposition (B1), and (b) bidirectional deposition (B2) and (c) bidirectional high power condition (B3).
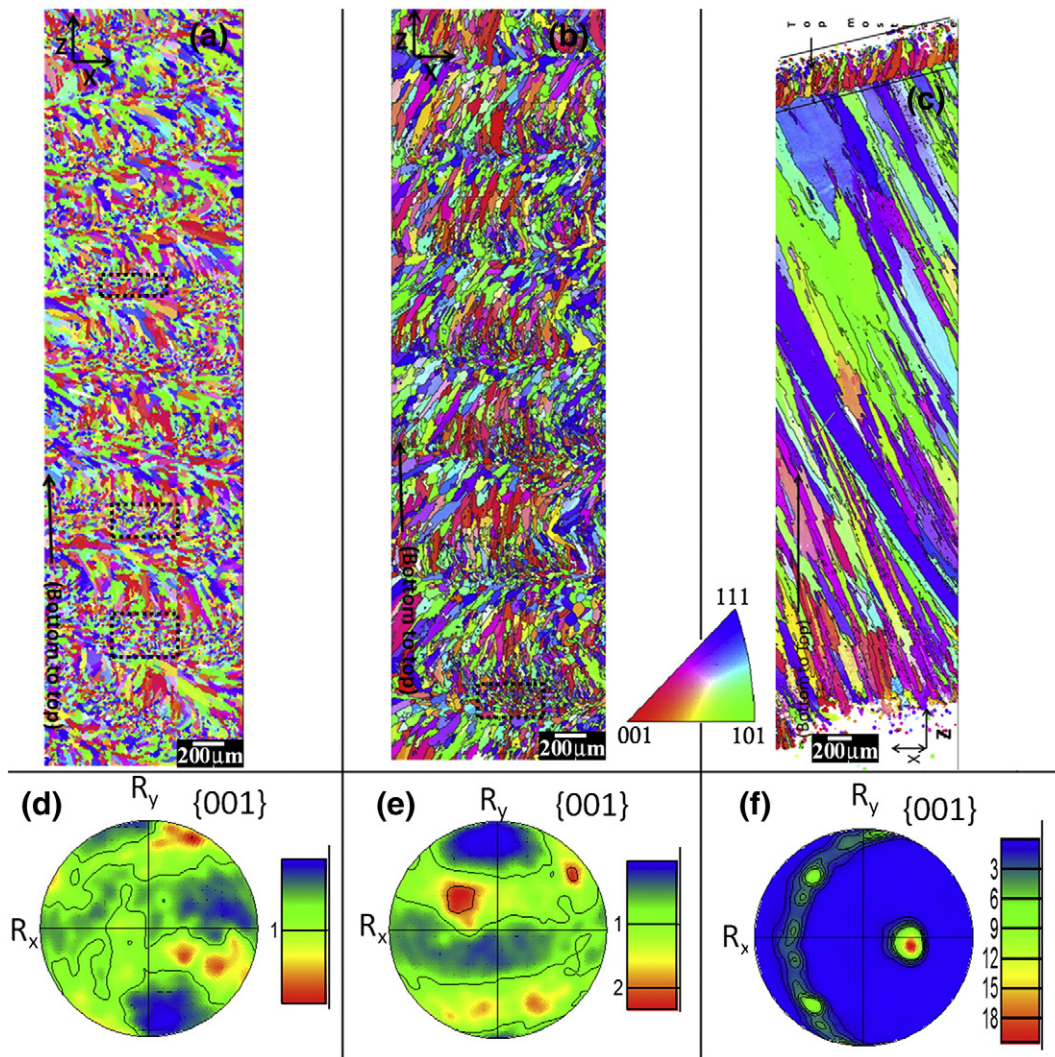
Fig. 7 – EBSD maps for B1 (a), B2 (b) and B3 (c), and their respective {100} pole figures (d, e, and f). The dotted boxes in (a) and (b) show the equiaxed grain regions.

growth of dendrites [16] where a lower G/R ratio would provide columnar growth. Studies by Gäumann et al. showed that an increase in laser power would lead to higher G/R value, promoting equiaxed growth. More recent work by Pinkerton et al. [17] suggested that the microstructural development due to laser deposition is possibly more complex than previously thought by Gäumann et al., and that other influences are equally important (e.g. local fluctuations in G due to Marangoni flow and in nucleation density due to the injected powder).

In the current study, complete re-melting of the previous layer at lower laser powers is limited by the heavy heat suction from the cold. Although columnar grain structure is observed within the layers at lower laser powers as suggested by Gäumann et al. [16], the grains are not completely columnar throughout the build. The fine grain zone between layers was found to disappear as the build height increased. Heat accumulation in the build was previously measured by Pinkerton et al. in thin-walled Waspaloy builds using thermal imaging [17]. Nonetheless, single crystal microstructure or large directionally solidified columnar grain structure was not achieved. It is important to point out that the differences in the ranges of the process parameters between the

various studies can make it difficult to draw general conclusions on the influence of the process parameters on the columnar-equiaxed development.

The (001) pole figures of B1 and B2 (Fig. 7d and e, respectively) samples showed a generally weak average texture (covering the entire build, 1–2× random). In B3 (Fig. 7f), the build shows a strong texture (20× random), where the microstructure resembles a directionally solidified structure, with a preferred orientation whereby the grains grew epitaxially parallel to the (001) planes parallel to the direction of the maximum thermal gradient, as this is the crystallographically favoured orientation for FCC alloys [18]. Fibre texture in Ni-superalloys DLF builds was previously observed by Moat et al. even when a pulsed beam laser was used [19,20]. The grains tend to tilt towards the resultant heat flux direction, which is from the side to the centre of the deposit, as the sides are cooler than the centre due to convection losses.

It is important to note that the substrate was a rolled IN718 sheet, with a uniform fine grain rolled structure. Following the initial pre-scan the first microstructure layers at the build-substrate form by epitaxial growth from existing grains.
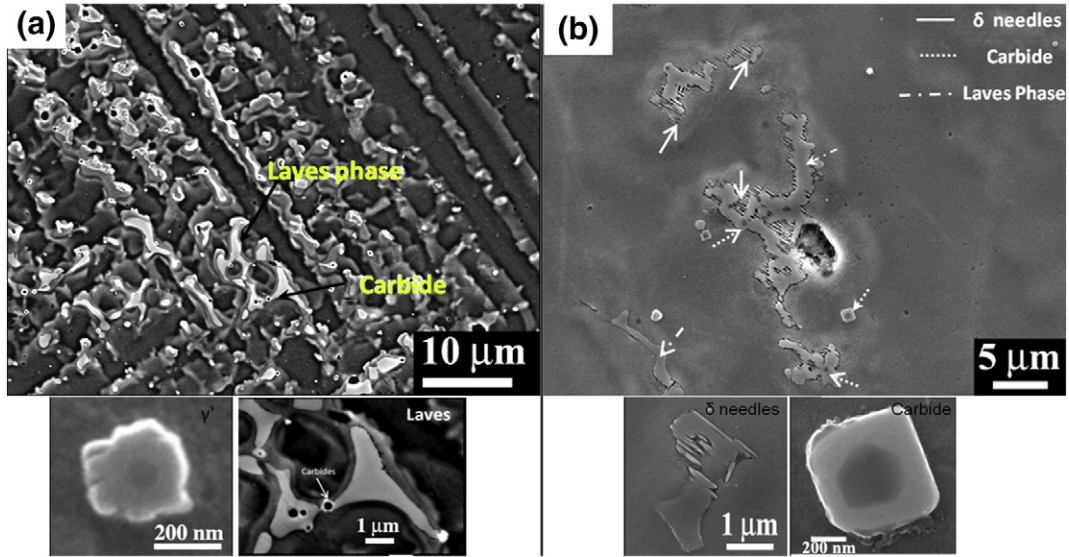
Fig. 8 – BSE SEM micrographs showing the intermetallic precipitates in (a) B2 (lower inset shows the γ′ and Laves phases at higher magnification) and (b) B3 (lower inset shows the δ needles at stacking faults and carbides at higher magnification).

As reported by Hofmeister et al. [9], high laser powers are associated with lower cooling rates, and the melt pool temperature gradually rises with increase in the build height due to the reduction of the heat sink effect of the substrate. As a result, the grain structure gets coarser with increase in the build height. Furthermore, it would be expected that the high melt pool temperature and the continuous heat flux during the bidirectional high power deposition would lead to complete re-melting of the successive layers, leading to epitaxial growth of the grains. Eventually, the heat input will be discontinued at the final layer, leading to rapid cooling, and hence breaking this large columnar grain structure.

3.4. Precipitates structure

DLF generates a very different precipitate structure, from that in cast or wrought structures, due to the rapid solidification associated with DLF. Generally, in B1 and B2 the build microstructures showed a dendritic microstructure, with considerable heavy element segregation within the dendrites as is apparent from the contrast levels in the BSE images (Fig. 8a). White irregularly shaped phases were observed in the inter-dendritic regions. The size of these phases was

~1–2 μm. EDS analysis (Fig. 9) showed that the phase is rich in Nb, Mo and Ti, the principal elements of the Laves. Furthermore, the area around this phase was also Nb-rich (segregation in Fig. 9b) compared to the matrix. Laves phases are irregularly shaped phases which form due to Nb segregation with the other alloying elements with a typical composition of (Ni, Fe, Cr) $_2$(Mo, Nb, Ti), instead of γ″ (Ni$_3$Nb). Previously Qi et al., observed precipitates with similar morphology and composition in DLF builds, and this was confirmed as Laves phase [13]. This phase is detrimental to mechanical properties but it can be dissolved in the matrix by proper heat treatments. Other than Laves, a few square and spherical shaped (around 200–300 nm) precipitates rich in Ti and Nb (carbide in Fig. 9b) are also observed which could be carbides.

Some differences in the phase structures were observed in the high power build B3 (Fig. 8b). It was observed that they are elongated and oriented in the direction of grain growth (i.e., the solidification direction). The Laves particles were larger, with less obvious diffused etch response around the precipitate when compared to the low power builds. The size of these Laves particles was around ~20–30 μm, with few of them as long as 100 μm, which could affect the liquation crack sensitivity [21]. EDS analysis showed that precipitates are Nb and Mo-rich

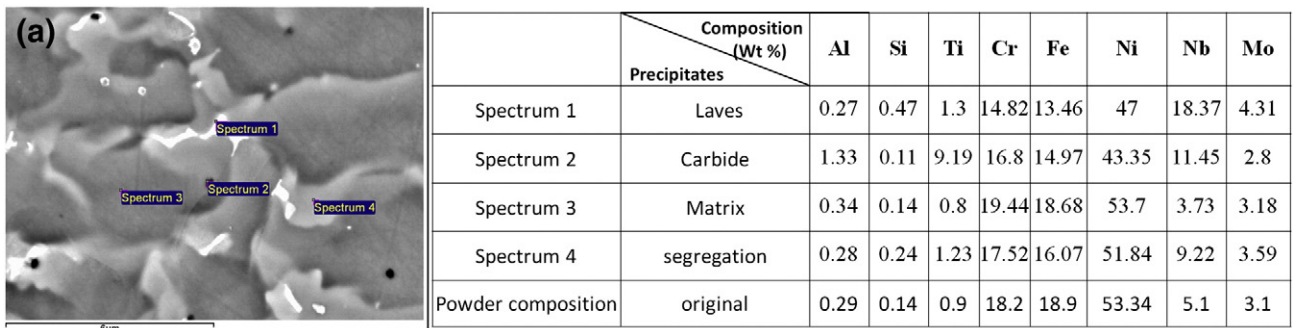| Composition (Wt %) / Precipitates		Al	Si	Ti	Cr	Fe	Ni	Nb	Mo
Spectrum 1	Laves	0.27	0.47	1.3	14.82	13.46	47	18.37	4.31
Spectrum 2	Carbide	1.33	0.11	9.19	16.8	14.97	43.35	11.45	2.8
Spectrum 3	Matrix	0.34	0.14	0.8	19.44	18.68	53.7	3.73	3.18
Spectrum 4	segregation	0.28	0.24	1.23	17.52	16.07	51.84	9.22	3.59
Powder composition	original	0.29	0.14	0.9	18.2	18.9	53.34	5.1	3.1

Fig. 9 – (a) BSE SEM micrograph of sample B2 showing a number of EDS point scans, and their respective chemical compositions of the various precipitates.
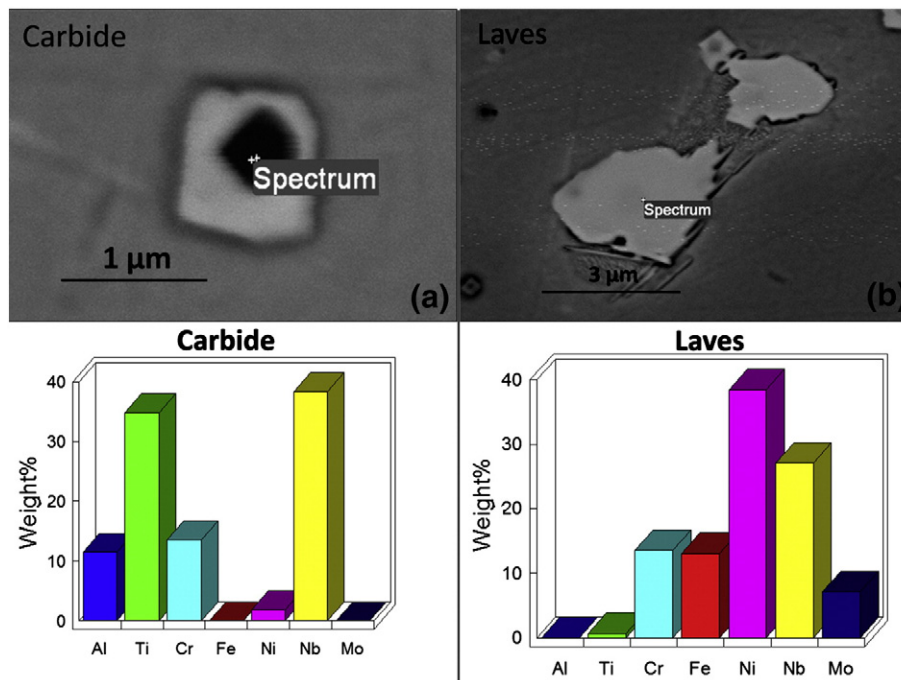
Fig. 10 – EDS of sample B3 showing the composition of carbide and the Laves phases.

(Fig. 10), suggesting them to be Laves. A few interesting features were also observed in this phase. First, fine carbides were embedded in them. Second, there were needle-like structures protruding from these phases, which resemble the δ phase morphology [12]. These were also observed by Clark et al. in MIG (metal inert gas) SMD process [22]. In general, precipitation of δ phase occurs following ageing for less than 100 h at a temperature range of 750 °C to 1000 °C with maximum precipitation at 900 °C at the grain boundaries. Azadian et al. [12] stated that δ precipitation can start at lower temperatures at stacking faults in the γ'' phase. Because of the high laser power and the continuous heat input, the build layers could possibly stay at high temperatures for a considerable time [23], leading to the formation of δ needles at the stacking faults. These needles were not observed in B1 or B2 due to lower heat input, which was not enough for these needles to nucleate. Although δ phase is generally detrimental for the mechanical properties, proper morphology of these precipitates at grain boundaries could improve the creep property of these materials [24]. The inset in Fig. 7b also shows the shapes of carbides and δ precipitates. The fine square-shaped particles, which are Ti and Nb-rich (Fig. 10), could be carbides (500 nm).

4. Conclusions

For laser deposited thin walled samples it was found that

1. The deposited samples had low porosity levels of about 0.2% which increased to 0.8% with increase in laser power.
2. At the lower laser powers the microstructure was a mixture of fine and coarse grains, with only a weak texture, but at higher power a strongly <100> textured columnar structure was formed i.e., variation in laser power showed a significant variation in grain structure and grain size of direct laser fabricated samples.
3. With increase in laser power, the Laves phase particles become far larger and needle-shaped δ phase and carbides start to appear on them.

Acknowledgements

R E F E R E N C E S

[1] Schlienger E, Dimes D, Griffith M, Michael J, Oliver M, Romero T, et al. Near net shape production of metal components using LENS. Proceedings of the Third Pacific Rim International Conference on Advanced Materials and Processing, Honolulu, HI; 1998. p. 1581.

[2] Wu X, Mei J. Near net shape manufacturing of components using direct laser fabrication technology. Journal of Materials Processing Technology 2003;135(2–3):266–70.

[3] Qi H, Azer M, Singh P. Adaptive toolpath deposition method for laser net shape manufacturing and repair of turbine compressor airfoils. The International Journal of Advanced Manufacturing Technology 2010;48(1):121–31.

[4] Blackwell PL. The mechanical and microstructural characteristics of laser-deposited IN718. Journal of Materials Processing Technology 2005;170(1–2):240–6.

[5] Tabernero I, Lamikiz A, Martínez S, Ukar E, Figueras J. Evaluation of the mechanical properties of Inconel 718 components built by laser cladding. International Journal of Machine Tools and Manufacture 2011;51(6):465–70.

[6] Zhao X, Chen J, Lin X, Huang W. Study on microstructure and mechanical properties of laser rapid forming Inconel 718. Materials Science and Engineering: A 2008;478(1–2):119–24.

[7] Dinda GP, Dasgupta AK, Mazumder J. Laser aided direct metal deposition of Inconel 625 superalloy: microstructural evolution and thermal stability. Materials Science and Engineering: A 2009;509(1–2):98–104.

[8] Sexton L, Lavin S, Byrne G, Kennedy A. Laser cladding of aerospace materials. Journal of Materials Processing Technology 2002;122(1):63–8.

[9] Hofmeister W, Wert M, Smugeresky J, Philliber JA, Griffith M, Ensz M. Investigating solidification with the laser-engineered net shaping (LENSTM) process. JOM 1999;51(7):1–6.

[10] Carlson RG, Radavich JF. Microstructure characterization of cast 718: superalloy 718—metallurgy and applications. In: Loria EA, editor. The Minerals, Metals and Materials Society; 1989. p. p79–95.

[11] Radavich JF. The physical metallurgy of cast and wrought alloy 718. Superalloy 718—metallurgy and applications. Warrendale: TMS; 1989.

[12] Azadian S, Wei L-Y, Warren R. Delta phase precipitation in Inconel 718. Materials Characterization 2004;53(1):7–16.

[13] Qi H, Azer M, Ritter A. Studies of standard heat treatment effects on microstructure and mechanical properties of laser net shape manufactured Inconel 718. Metallurgical and Materials Transactions A 2009;40(10):2410–22.

[14] Suman D, Fuesting TP, Danyo Gr, Brown LE, Beaman JJ, Bourelli DL, et al. Direct laser fabrication of a gas turbine engine component—microstructure and properties—part I. SFF Symposium Proc; 1998.

[15] Flemings MC. Solidification processing. McGraw-Hill; 1974.

[16] Gäumann M, Bezençon C, Canalis P, Kurz W. Single-crystal laser deposition of superalloys: processing–microstructure maps. acta materialia 2001;49(6):1051–62.

[17] Pinkertona AJ, Karadge M, Syed WUH, Li L. Thermal and microstructural aspects of the laser direct metal deposition of waspaloy. Journal of Laser Applications 2006;18(3):216.

[18] Roger RC. The superalloys: fundamentals and applications. NY: Cambridge University Press; 2006 327 [USA].

[19] Moat RJ, Pinkerton AJ, Li L, Withers PJ, Preuss M. Crystallographic texture and microstructure of pulsed diode laser-deposited waspaloy. Acta Materialia 2009;57(4):1220–9.

[20] Andrew PJ, Moat R, Li L, Preuss M, Withers PJ. Diode laser metal deposition: the effect of pulsed beam parameters on superalloy microstructure and deposit morphology. 25th International Congress on Applications of Lasers and Electro-optics (ICALEO), Scottsdale, AZ, USA; 2006.

[21] Dye D, Hunziker O, Reed RC. Numerical analysis of the weldability of superalloys. Acta Materialia 2001;49:683–97.

[22] Clark D, Bache MR, Whittaker MT. Shaped metal deposition of a nickel alloy for aero engine applications. Journal of Materials Processing Technology 2008;203(1–3):439–48.

[23] Clark D, Bache M, Whittaker M. Microstructural characterization of a polycrystalline nickel-based superalloy processed *via* tungsten-inert-gas-shaped metal deposition. Metallurgical and Materials Transactions B 2011;42(2):434.

[24] Sjfberg G, Ingesten N. Grain boundary Y-phase morphology, carbides and notch rupture sensitivities of cast alloy 718. Superalloy 718—metallurgy and applications. Warrendale: TMS; 1991.